UNICA UNIVERSITÀ DEGLI STUDI DI CAGLIARI

UNICA IRIS Institutional Research Information System

This is the Author's accepted manuscript version of the following contribution (in bold face the UNICA contributors):

Payal Wadhwa and **Alessio Filippetti**

Fully spin-polarized, two-dimensional hole and electron gases at the highly-polar (111) EuTiO3/SrTiO3 interface

ACS Appl. Electron. Mater. 2024, 6, 3657−3665

The publisher's version is available at:

https://doi.org/10.1021/acsaelm.4c00344

When citing, please refer to the published version.

This full text was downloaded from UNICA IRIS https://iris.unica.it/

Fully spin-polarized, two-dimensional hole and electron gases at the highly-polar (111) $EuTiO_3/SrTiO_3$ interface

Payal Wadhwa[1] and Alessio Filippetti,[1,2]*

1 Dipartimento di Fisica, Università di Cagliari. S.P. Monserrato Sestu Km.0,700. Monserrato (Ca) 09042-I, Italy
2 CNR-IOM, Istituto Officina dei Materiali, Consiglio Nazionale delle Ricerche, S.P. Monserrato Sestu Km.0,700. Monserrato (CA) 09042-I, Italy

[*] Corresponding author: alessio.filippetti@dsf.unica.it

Keywords: 2D charge confinement, oxide heterostructure, magnetic materials, ab-initio calculations, polar materials, spintronics

ABSTRACT

The first experimental observation of two-dimensional hole gas in (001) $SrTiO_3/LaAlO_3/SrTiO_3$ heterostructures with carrier mobilities ~10^3 cm^2/Vs at low temperature, has opened innovative avenues for future oxide electronics, and demonstrated that the elimination of point defects is instrumental to achieve spontaneously confined hole carriers. Stimulated by these findings, we analyze the highly polar (111) orientation of $SrTiO_3$ and $EuTiO_3/SrTiO_3$ structures. Using first-principles calculations, we show that tightly confined and fully spin-polarized hole and electron gases can be realized at the *p*-doped and *n*-doped terminations of these structures, respectively. The high polarity is key to achieve strong, spontaneous carrier attraction towards the surface, provided that the macroscopic fields generated by the polarity in the interior of the material are efficiently screened out. Our findings candidate the (111) $EuTiO_3/SrTiO_3$ interface as a credible material for innovative spintronic applications, even capable to outperform its (001) counterpart.

Introduction

Transition metal oxide heterostructures have come through an extraordinarily intense research activity in the last 20 years or so, driven by an exciting variety of novel physical phenomena observed at their surfaces and interfaces. The golden age of modern oxide electronics was boosted, first and foremost, by the discovery of a 2D electron gas (2DEG) at the $LaAlO_3/SrTiO_3$ (LAO/STO) interface[1-3] exhibiting extraordinary features like high T_c superconductivity,[4,5] large negative magnetoresistance,[6] Rashba Spin-orbit coupling.[7] However, some crucial features of the 2DEG formation have puzzled scientists over the years. A critical aspect concerns the lack of a 2D hole-gas (2DHG) counterpart, which is a severe drawback to the practical implementation of an oxide-based nanoelectronics. Past works[8,9] suggest that this aspect may descend from the disruption of the perfect surface epitaxy due to structural disorder. In fact, direct observation of 2DHG was recently reported in (001) STO/LAO/STO heterostructures[10] and at the (001) STO surface,[11] and it was made evident that a very high level of structural order is instrumental to the presence of the hole gas.

Another much debated aspect concerns the presence of ferromagnetic (FM) order in 2DEG's which, despite intensive research over the years, was revealed very elusive. Traces of magnetisms observed in STO and LAO/STO are typically attributed to non-intrinsic origin, while the insertion of magnetic layers at the interface often results in the disruption of 2DEG characteristics. At our knowledge, the only clear evidence of FM order was observed in a variety of $EuTiO_3$ (ETO) heterostructures, specifically the (001) LAO/ETO/STO interface,[12-16] the (001) and (110) ETO surface,[17-19] and the (111) LAO/ETO/STO interface.[20,21] This encouraging scenario motivated us to explore the pristine properties of (111) ETO/STO heterostructures: on the one hand, ETO can enable robust FM behavior; on the other, the still scarcely explored (111) termination, with its highly polar Ti and SrO_3 alternate stacking, represents in principle a strong push towards robust, spontaneous charge confinement. In comparison, intrinsic confinement in non-polar (001) surfaces[22-25] can only rely on much weaker surface polarization effects.

The (111) termination is challenging from the experimental viewpoint since polarity makes the surface unstable and prone to various compensation mechanisms. Several structural reconstructions controlled by annealing time, temperature and oxygen pressure were reported,[26-28] but 1×1 unreconstructed surfaces with perfectly flat terraces were observed as well.[29-32] In particular, the first STM images and RHEED analysis of the (111) STO surface obtained by UHV annealing showed the presence of both SrO_{3-x} and Ti terminations.[29] A

different procedure, based on chemical etching and oxygen annealing was used to produce Ti-rich 1×1 (111) STO surfaces.[30-32] In absence of reconstructions, other polar-compensating mechanisms should occur. A variety of optical[33-34] and magnetoelectric[35,36] measurements revealed the presence of a 2DEG at the unreconstructed surface, attributed to oxygen vacancies in the substrate. In fact, the excess electrons produced by oxygen vacancies can migrate to the surface to generate the electron gas and simultaneously erase the electrostatic divergence. A similar charge transfer mechanism may act in the generation of the 2DEG observed in (111) STO/LAO interfaces,[37-42] and (111) $SrIrO_3/SrTiO_3$ interfaces,[43] with RHEED and STEM images showing ordered structures and flat terraces.

The theoretical literature about (111) termination of STO surface,[34,35,44-48] LAO/STO interface,[35,40-42,49-51] and STO bilayers[52] is abysmally smaller than that for the (001) analogues. In fact, for ab-initio supercell simulations, polarity is a major obstacle since it produces spurious electric fields which must be somehow compensated. In addition, a stoichiometric supercell necessarily includes both *n*-type and *p*-type terminations, thus mixing up in a cumbersome way their properties. For these reasons, the near totality of theoretical studies is carried out using tight-binding models drawn on the basis of (111) bulk symmetry, thus without including the actual surface simulation. To circumvent these obstacles, here we performed our calculations using the structures illustrated in Figure 1, which include one additional monolayer to the perfect stoichiometry. Experimentally, this mimic a situation where the (111) slab is cleaved from bulk with the same termination on both sides. In this way the bulk polarity is compensated, and charge confinement only comes from genuine surface or interface effects. The additional monolayer also furnishes excess electrons (for Ti termination) or holes (for SrO_3 termination) which may be assumed as coming from various possible sources (e.g. oxygen vacancies, doping, or even field-effect). We will show that in this structural setting which only capture pristine conditions, a spontaneous band bending occurs due to surface polarity, causing both electrons and holes to remain confined within a few layers from the surface. Furthermore, both 2DEG and 2DHG are found to be fully spin-polarized, consistently with the robust ferromagnetism found in *n*-doped ETO bulk for a wide variety of dopants,[53–60] and in ETO-based heterostructures.[12-21] These results furnish sound evidence that the (111) ETO/STO interface presents highly favorable characteristics to the spontaneous formation of tightly confined and robustly spin-polarized 2DHG and 2DEG; as such, it can be a valuable building block for the implementation of an oxide-based spintronic nanotechnology.

Methodology

Ab-initio calculations are performed within the framework of Density Functional Theory, as implemented in the VASP code.[61] Projected augmented wave[62] basis set with a cut-off energy of 550 eV and generalized gradient approximation[63] with Hubbard interaction[64] (GGA+*U*) are used, with on-site Coulomb repulsion $U = 4\ eV$ and 7.5 *eV* for Ti 3*d* and Eu 4*f*, respectively, in consistency with previous theoretical reports.[16,60] Γ-centred Monkhorst-Pack scheme and *k*-point mesh of 20×20×1 are used. Structure optimization is performed only along the *z*-direction, with a fixed in-plane lattice constant equal to that of STO bulk ($a_0 = 3.905\ \AA$), while atoms are fully relaxed up to a force threshold of 1 *meV/Å*.

Results and Discussions

We start the analysis from the SrO_3-terminated STO surface and the EuO_3-terminated ETO/STO interface. For the former we use the symmetric vacuum/STO and vacuum/ETO/STO trigonal supercells sketched in Figure 1a, the latter with two ETO layers per surface.

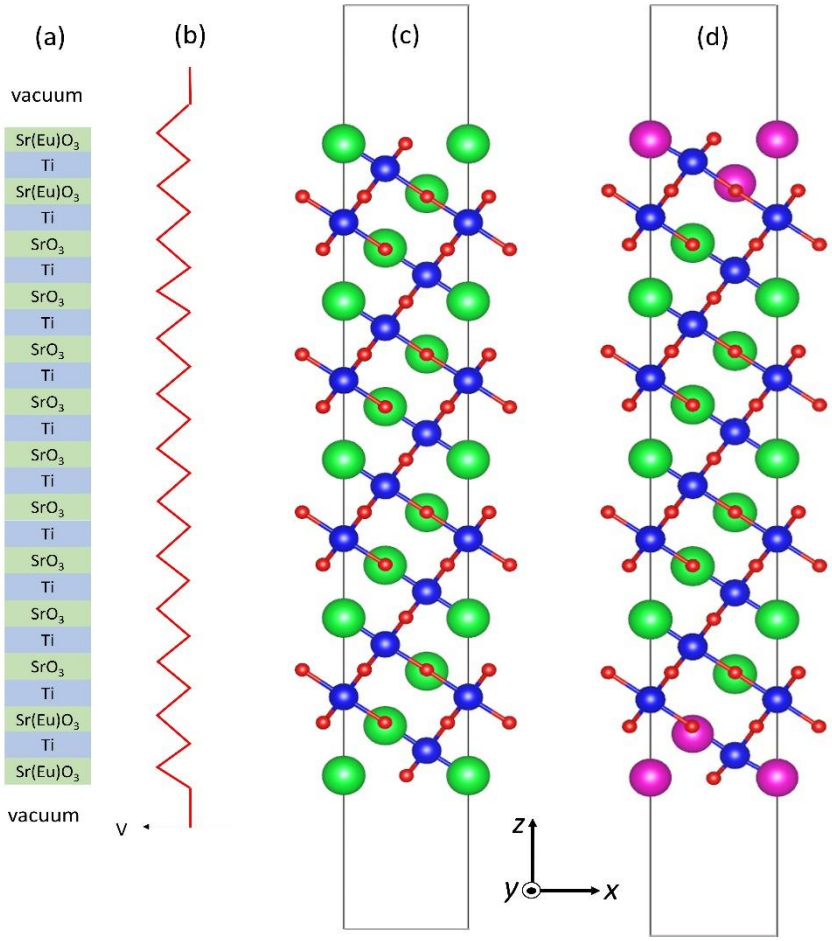

Figure 1: a) Schematic diagram of the $Sr(Eu)O_3$-terminated (111) structures. b) the corresponding electrostatic potential given by the alternating Ti^{+4} and $[Sr(Eu)O_3]^{-4}$ charged plane stacking. c) actual atomic structure for the

SrO_3-terminated STO surface after atomic structure relaxation. d) same for the EuO_3-terminated ETO/STO interface. Color code is green (Sr), magenta (Eu), blue (Ti), red (O). In trigonal symmetry *x*, *y*, *z* correspond to the $[1\bar{1}0]$, $[01\bar{1}]$ and $[111]$ axes of the cubic symmetry, respectively; *y* is perpendicular to the page, and *x* is at 120° from *y*.

Figure 1b displays the electrostatic potential generated by the alternance of +4 and -4 charged planes. Inversion symmetry with respect to the central SrO_3 layer prevents the electrostatic build up and the rise of unphysical electric fields across the slab and in the vacuum. In Figure 1c and 1d the actual atomic structures are shown, calculated after atomic relaxations and *z*-axis optimization. We notice that the adopted (1x1) planar symmetry rules out antiferrodistortive oxygen rotations which are known to tightly compete with polar distortions at the (001) LAO/STO interface.[65] This is a reasonable assumption since, unlike LAO, ETO is simple cubic at room-T, while the oxygen tilting which characterize the low-T *I4/mcm* tetragonal phase are too minimal[66] to have any significant impact on the electronic structure.

Charge neutrality compensates the presence of the additional SrO_3 monolayer with a built-in doping charge of 4 holes, i.e. 2 holes per surface. A key question is whether this excess hole charge is bi-dimensionally confined or homogeneously spread throughout the substrate. This can be clearly revealed by the layer-resolved orbital-projected DOS, plotted in Figure 2; for clarity, only the most fundamental orbitals (O 2*p*, Ti 3*d*, and Eu 4*f*) are shown, further separated in up-spin (positive) and down-spin (negative) contributions. Looking at Figure 2a, and following the valence band top (VBT) profile across the layers from the figure bottom to the top, we can immediately visualize how the hole charge is redistributed: at the bottom (corresponding to the 6th STO layer below SF) the VBT is aligned to the Fermi level (E_f), thus no holes are present at this deepness, and the DOS is bulk-like and insulating. Moving towards the surface, the VBT rises above E_f and the hole DOS shows up starting from layer SF-3. Specifically, we found ~80% of the holes present in the surface layer (SF), ~12% on the sub-surface layer (SF-1), and the remaining portion in SF-2 and (very marginally) in SF-3, thus the 2DHG is entirely confined in just 3-4 layers from the surface. We estimate from our calculations an upward band disalignment of ~0.5 eV at the SF layer, with respect to the bulk VBT. For what concerns the orbital characters, the holes are almost entirely located on the O 2*p* states, with a marginal (~3%) contribution from the Ti *3d* states (detail of the charge distribution is given in Table S1). Remarkably, we obtain that the hole gas is fully spin-polarized, since the holes entirely seat in a single O 2*p* spin channel, i.e. the surface is half-metallic. Since all the holes are in the positive (up-spin) channel, an overall down-spin magnetization of 2 μ_B per (1×1) surface is present in the system. This spin-polarization is purely consequence of the tight charge

confinement and the resulting Coulomb repulsion of the O 2*p* states in the vicinity of the surface.

Now we come to analyze the EuO_3 termination (Figure 2b), for which two Eu layers are included in place of two Sr. This choice is made in analogy with the (001) LAO/ETO/STO interface, for which the spin-polarized 2DEG is observed for ETO thickness of no more than 2 unit cells.[12-15] Analogously to the SrO_3 surface, the O 2*p* VBT is aligned to E_f at the slab center, and then it crosses E_f while approaching the surface, thereby indicating the presence of a strongly confined 2DHG. However, the presence of the Eu 4*f* orbitals makes this 2DHG different and way more interesting than that at the (111) STO surface.

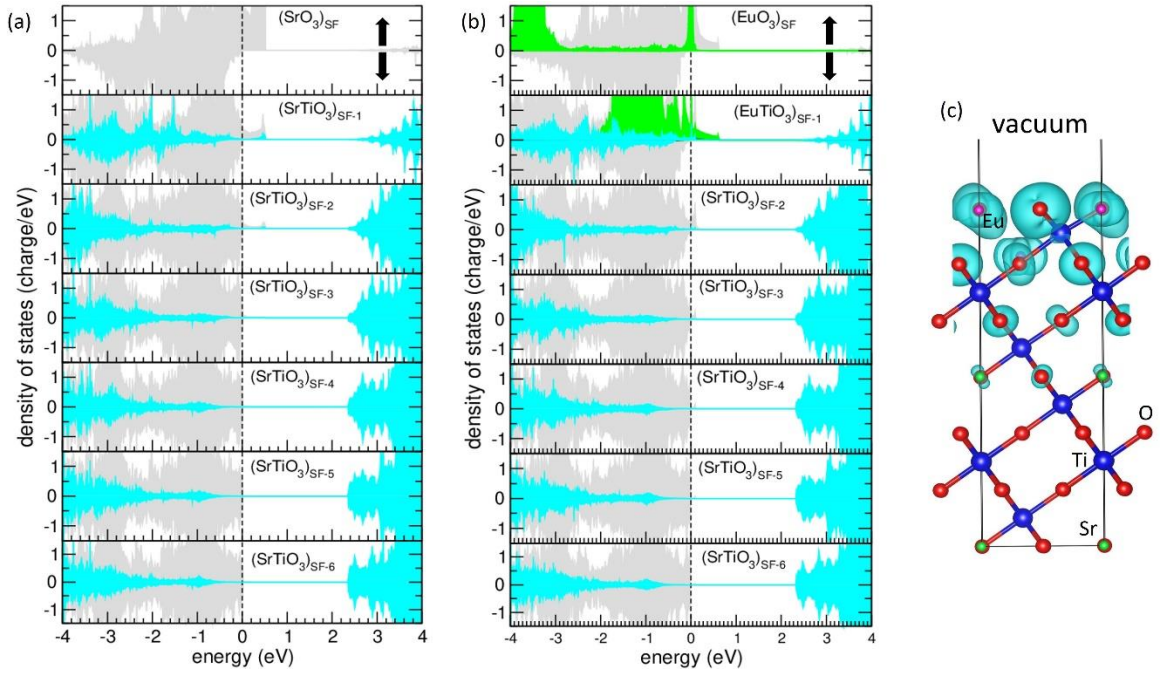

Figure 2: a) Orbital-projected DOS of the SrO_3-terminated STO surface. Each graph corresponds to a specific (111) atomic layer of the slab; the inmost (i.e. most bulk-like) $SrTiO_3$ layer is at the bottom (labelled SF-6), the surface SrO_3 layer (SF) is at the top. Positive and negative DOS indicate up-spin and down-spin components. Orbitals shown are O 2*p* (shaded gray) and Ti 3*d* (cyan). The vertical dotted line indicates E_f and is aligned to zero energy. b) Same quantities and same graph arrangement for the EuO_3-terminated ETO/STO interface. Orbital color code is O 2*p* (shaded gray), Eu 4*f* (green), Ti 3*d* (cyan). c) Hole density isosurface (drawn in light blue) for the ETO/STO interface, calculated from the electronic states lying in 1 eV region above E_f.

It is worthy to point out that in bulk ETO the Eu 4*f* states are fully spin-polarized, with an extra-large (~12 eV) spin-splitting, and ~7 μ_B magnetic moment on each Eu.[59,60] Most importantly, in bulk ETO the spin-majority Eu 4*f* bands lie at the VBT and are visibly separated from the broad O 2*p* band manifold placed at lower energy. Here the surface produces some dramatic effects in the electronic properties: the O 2*p* states in the EuO_3 SF layer undergo a large (~ 1

eV) spin splitting, which brings them to largely overlap with the Eu 4*f* states in the spin-majority channel. In fact, we see a sharp (~ 0.3 eV wide) 4*f* DOS peak crossed by E_f, superimposed to a broad (~ 2 eV wide) O 2*p* DOS feature. The SF-1 layer, on the other hand, shows a ~ 2.0 eV-wide 4*f* DOS peak cut by E_f, lying ~2 eV below the conduction band bottom (CBB), in agreement with photoemission measurements for the (001) ETO surface.[17] Remarkably, the holes are only present in the spin-majority (positive) channel, i.e. the 2DHG is fully spin-polarized, with 2 μ_B magnetization per (1×1) surface. Unlike the 2DHG in the STO surface, which is purely originated by O 2*p* states, this 2DHG is given by a broad admixture of Eu 4*f* and O 2*p* states. Furthermore, this 2DHG magnetization now contributes to reduce (i.e. is oppositely oriented to) the bulk-like, up-spin contribution of the Eu magnetic moments, so that the overall ETO/STO magnetization amounts to ~6 μ_B per ETO layer. Figure 2c displays an isosurface of the 2DHG spatial distribution obtained from the bands lying within 1 eV above E_f, which gives an immediate feel of the fast hole charge decay with the distance from the surface. Being fully spin-polarized, this hole charge is tantamount to the 2DHG magnetization density.

In Figure 3 the band energies calculated for the STO surface and the ETO/STO interface are presented; in order to highlight the 2DHG characteristics, the bands including some hole fractions are drawn in blue; also, only a narrow energy window around the VBT is considered. For the STO surface we have 3 bands hosting the 2DHG, the highest in energy being very flat and mostly derived by an O p_z surface state. Degenerate with the latter at the Γ point, there is a second O *2p* band with effective mass m^* =1.13 m_e in direction Γ-*M*, and a third O *2p* band slightly lower in energy, with m^* =1.04 m_e. These values are consistent with the typical effective masses for bands of *2p* orbital character. For what concerns the ETO/STO interface, the situation appears more favorable to hole mobility, since most of the 2DHG is hosted by a single, broad O *2p* band, which runs across the whole Brillouin zone with m^* =0.77 m_e at the Γ point. At lower energy we find other two bands with m^* =1.13 m_e and 1.04 m_e at Γ point. They are

derived by a strong admixture of Eu 4*f* and O 2*p* orbitals; we can notice the flat band segment located right at E_f, corresponding to the Eu 4*f* DOS peak present in the subsurface ETO layer.

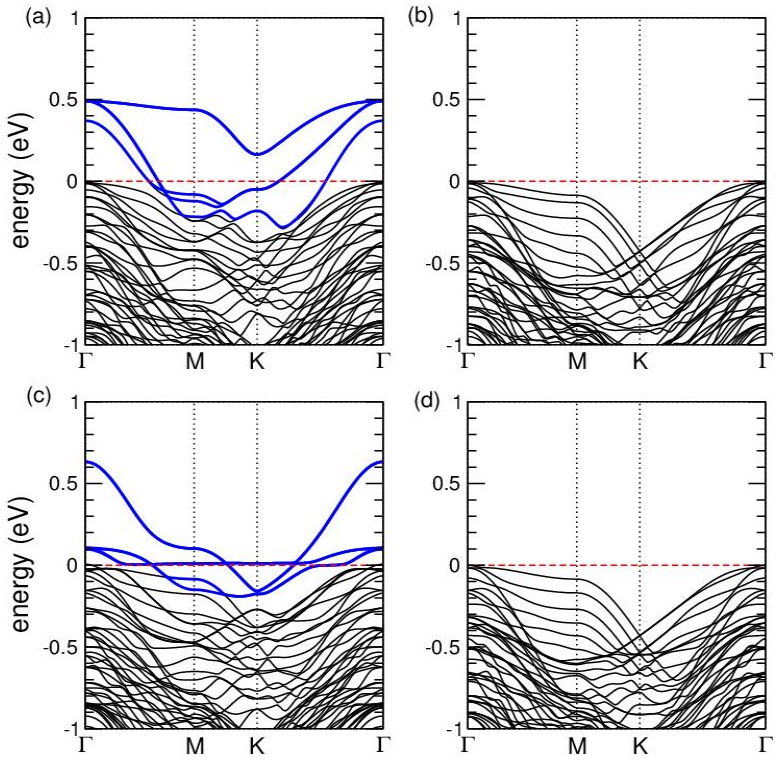

Figure 3. a), b): Band energies of the SrO_3-terminated STO surface, separated in up-spin (a) and down-spin (b) channels. The hole bands are drawn in blue; the dashed red lines indicate the Fermi energy. (c), (d): same as before for the EuO_3-terminated ETO/STO interface.

We emphasize that the presence of a hole gas with fairly mobile and fully spin-polarized carriers at the VBT is a fortunate and rare occurrence, since strong spin-polarization typically derives from highly localized (e.g. 3*d* and 4*f*) orbitals. Here two key factors explain the peculiarity of this hole gas: the strong O 2p - Eu 4*f* orbital hybridization, and the narrow charge confinement occurring at the (111) surface, which is much stronger than in the more familiar (001) titanates, where the 2DEG's typically spread across thickness of several nm. In turn, this extreme confinement can be traced back to the high polarity of the (111) surfaces. To show the influence of polarity on confinement, we consider a linear chain model, with point charges Z = -4 located on each SrO_3 (or EuO_3) monolayer of the supercell, and Z = +4 on each Ti monolayer, and 2 additional holes on a specific SrO_3 (or EuO_3) monolayer. In Figure 4 the electrostatic energy of

the chain $E = \sum_{ij} Z_i Z_j / R_{ij}$ (here R_{ij} are distances between two point charges, and we take $e^2 / 4\pi\varepsilon_0$=1) is plotted as a function of the SrO_3 layer where the holes are localized; red and blue circlets refer to chains of increasing length. The dashed horizontal line (fixed to zero energy) corresponds to a configuration where the holes are completely unconfined and equally redistributed on each SrO_3 (or EuO_3) layer of the slab.

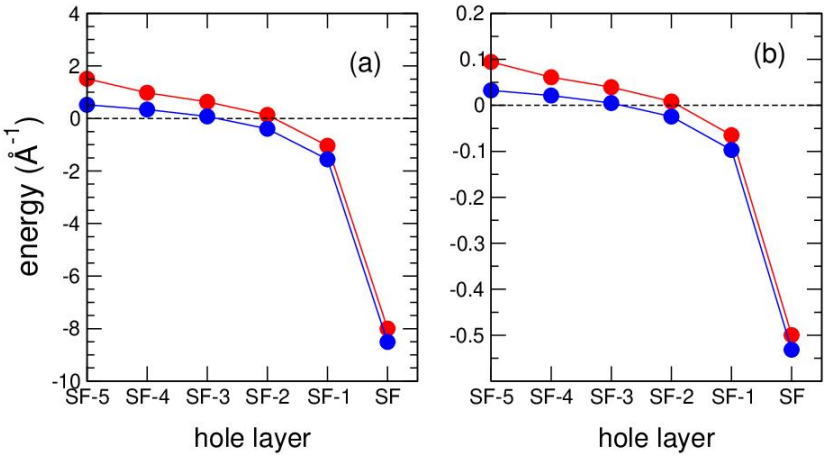

Figure 4. (a): Electrostatic energy of the ±4 point-charge chain model (see text), with two additional holes embedded in one of the SrO_3 layers. The hole location in the chain is indicated by the horizontal axis. The dashed line is a reference energy (aligned to zero) corresponding to the homogeneous hole distribution, with the 2 holes equally distributed on each -4 point-charge. Red and blue circles refer to chains of different length (25 and 37 point charges, respectively). (b) Same model for a hypothetical ±1 point-charge chain model, with 0.5 additional holes embedded in one of the -1 point-charges of the chain. Here the dashed line is the energy of the homogeneous distribution with the 0.5 holes equally distributed on each -1 point-charge.

We see from Figure 4a that placing the holes entirely on the fifth SrO_3 layer from the surface (SF-5) is less energetically convenient than spreading them homogeneously across the substrate; however, localizing the holes closer and closer to the surface, the chain progressively gains stability, until it becomes more stable than in the unconfined configuration. The reason is easily understood: the presence of holes reduces the layer polarity and in turn the electrostatic attraction between adjacent charges. This loss of stability is however reduced for holes located near the surface due to the proximity with the vacuum side, which reduces the bond coordination; thus the net effect is an intrinsic hole attraction to the surface. Notice that the model outcome is not an artifact of the small chain length (i.e. small number of layers in the supercell): in fact, for longer chain length (blue circles), the localized configurations gain

further stability over the homogeneous hole spread. In Figure 3b we show the result for the same point charge model, but with $Z = \pm 1$ (this can mimic, e.g., the AlO_2-terminated (001) LAO surface), and additional 0.5 holes per surface ensuring charge neutrality in the slab. We see that the qualitative behavior is completely analogous to the $Z = \pm 4$ case, but the energy gain of the surface-localized hole configuration (with respect to the homogenous distribution) is more than one order of magnitude lower than for $Z = \pm 4$. Clearly, stronger polarity means stronger drive to hole confinement at the surface. This concept can be more rigorously derived by the elegant formalism developed by Stengel for polar materials,[67] which relates the bending of the displacement field, and in turn charge confinement, to the value of formal polarization (i.e. 2e per unit surface for (111) ETO and STO layers).

Most of the arguments seen for the hole-doped SrO_3 and EuO_3 terminations also apply to the electron-doped Ti-terminated counterparts. The 2DEG presence at the (111) STO surface is reported in several previous works[20,33–36] (our results are shown in the Supplementary Information), thus hereafter we focus on the more interesting (111) ETO/STO interface. For the simulation we use a vacuum/ETO/STO supercell which includes two identical Ti surfaces, each with 2 electrons in excess (the optimized atomic structure is displayed in Figure 5a). The corresponding layer-resolved DOS (Figure 5b) displays a band bending at the surface which is oriented in the opposite verse with respect to that found at the SrO_3 termination. In fact, just like the negatively charged SrO_3 surface acts as attractive basin for holes, the positive Ti termination is attractive for electrons, so the conduction bands bend downward at the surface to capture the carriers in excess. This is clearly shown in Figure 5b: the CBB is above E_f for the bulk-like SF-6 layer, and well below E_f for the layers closer to the surface. Similarly to the 2DHG, this 2DEG is tightly confined within a narrow region of a few layers, and fully spin-polarized. Clearly, the point-charge chain model used to describe the hole gas gives identical results upon exchange of charge sign. On the other hand, the quantum chemistry of the electron gas is completely different, since the 2DEG is entirely hosted by Ti 3*d* orbitals. The (111)

orientation (cartesian axes are shown in Figure 5a) is characterized by a trigonal, anti-prismatic D_{3d} crystal field which splits the t_{2g} states in one a_{1g} singlet (i.e. d_{z^2}) and one e_g^{π} doublet (corresponding to a mixture of prevalent d_{xy}, $d_{x^2-y^2}$ and smaller d_{xz}, d_{yz} contributions). The orbital-resolved DOS (Figure 5c) shows the presence of one electron charge fully localized at the SF layer, lying at a very deep energy (from -1.5 eV to -2 eV), thus largely overlapping with the 4*f* DOS peak. Such a d_{z^2} dangling bond is likely going to be saturated by surface adsorbates (e.g. oxygens). The actual 2DEG is hosted by e_g^{π} states and spatially redistributed across the layers from SF to SF-2 in a ~0.4 eV wide energy window below E_f (layer-by-layer 2DEG decomposition is reported in Table S2). Remarkably, the 2DEG charge is entirely hosted in the down-spin Ti 3*d* channel, thus fully spin-polarized, with a magnetization verse opposite to that of Eu 4*f* magnetic moments. Strikingly, this configures a ferrimagnetic (FiM) half-metallic material, with an overall magnetization of ~6 μ_B per ETO layer (just like the EuO_3 termination). It is important to recall that bulk ETO is characterized by a tight competition between antiferromagnetic (AFM) and ferromagnetic (FM) exchange interactions mediated by the Ti 3*d* orbital overlap with Eu 4*f* and 5*d* orbitals.[59,60] This competition results in the AFM order for pristine ETO at low temperature, which is reverted to FM order upon inclusion of *n*-doping or in the LAO/ETO/STO interface. Here we can infer a qualitatively different mechanism which occurs in FiM half-metallic perovskites:[68] the large spatial overlap between itinerant Ti 3*d* and localized Eu 4*f* electrons makes their respective magnetic moments AFM-coupled, due to covalent superexchange; since Hund's rule forces the Ti 3*d* electrons to be spin aligned, the overall magnetic order is FiM, with E_f crossing the sole spin-minority Ti 3*d* DOS channel. This result is corroborated by the observation of ferromagnetic order in (111) LAO/ETO/STO,[20,21] with canted Ti 3*d* and Eu 4*f* magnetic moments (parallel in the surface plane and antiparallel orthogonally). We remark that these aspects are proper of the (111) heterostructure and set this 2DEG far apart from the electron gas observed in the *n*-doped (001) ETO/STO interface.

According to our analysis, the tight 2D confinement of the excess electrons near the surface is at the fundament of the peculiar magnetic behavior displayed by the (111) termination.

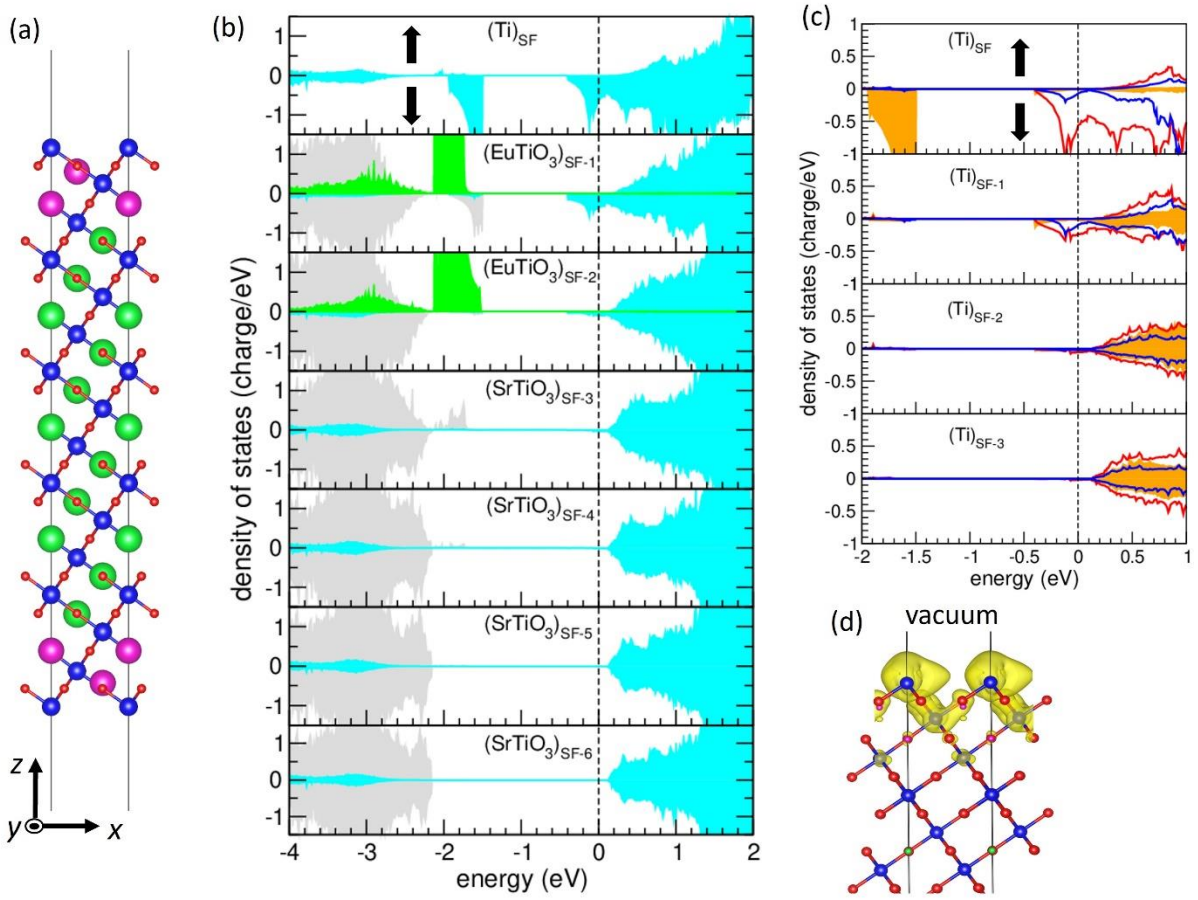

Figure 5: a) Atomic structure of the Ti-terminated (111) ETO/STO interface. Color code is green (Sr), violet (Eu), blue (Ti), red (O); *x*, *y*, and *z* axes are described in figure 1. b) Orbital-projected DOS. Each graph displays an atomic layer, with the surface Ti layer (SF) at the top, and the 6th $SrTiO_3$ layer (SF-6) at the bottom. Positive and negative DOS indicate up-spin and down-spin components. Orbitals are O 2*p* (shaded gray), Eu *4f* (shaded green), Ti 3*d* (shaded cyan). The vertical dashed line indicates the Fermi level and is aligned to zero energy. c) Orbital-resolved DOS of 3*d* states contributed by the Ti atoms of the 4 layers closer to the surface. Color code is red for the d_{xy}, $d_{x^2-y^2}$ doublet, blue for the d_{xz}, d_{yz} doublet, filled orange for the d_{z^2} singlet. d) Atomic structure with the 3D map of the 2DEG charge density isosurface drawn in yellow.

To display the 2DEG spatial distribution, in figure 5d we plot a charge density isosurface drawn from the occupied states lying within 1 eV below E_f, thus not including the d_{z^2} dangling bond at the surface. Just like for the 2DHG, this density also corresponds to the 2DEG magnetization density.

In Figure 6 the band energies of the (111) ETO/STO interface are displayed; the two excess electrons are hosted in the 3 bands drawn in blue. The lowest in energy corresponds to the d_{z^2}

dangling bond analyzed in the DOS; it runs across the whole Brillouin zone in the down-spin channel, well separated by all the other bands of the minority channel, and largely overlapping with the spin majority Eu 4*f* bands. The 2DEG resides almost entirely within the second-lowest band and (residually) within the third-lowest bands. As seen in the DOS, they derive from e_g^{π} states and display effective mass m^* =0.94 m_e at the Γ-point along the Γ-M direction. This value is slightly higher than the typical mass of the d_{xy} bands hosting the 2DEG in the (001) interfaces, since it is contributed by a mixture of the t_{2g} states of the octahedral O_h symmetry.

The bottom of these two bands at the Γ-point (-344 meV and -26 meV) displays a remarkable splitting from the bulk-like band manifold, located 171 meV above the Fermi energy (the SF-3 layer in Figure 5c). If compared with the trigonal band splitting obtained by X-ray linear dichroism for the *n*-doped termination of (111) LAO/ETO/STO and (111) STO,[20] our calculated values appear to be about an order-of magnitude larger. This indicates that the 2DEG charge in the calculations exaggerates that present in real samples, thus largely amplifying the surface band splitting with respect to the pure bulk-truncation effect. This is not surprising since alternative compensating mechanisms (e.g. cation mixing, surface adsorbates, charged point defects) can reduce the charge coming from pure electrostatic screening (the effect of charge confinement on the band splitting is further discussed in the Supporting Information). Finally, we obtain a large spin gap of 1.113 eV between spin-majority and spin-minority channels; this suggests that the large spin-polarization is stable against thermal fluctuations.

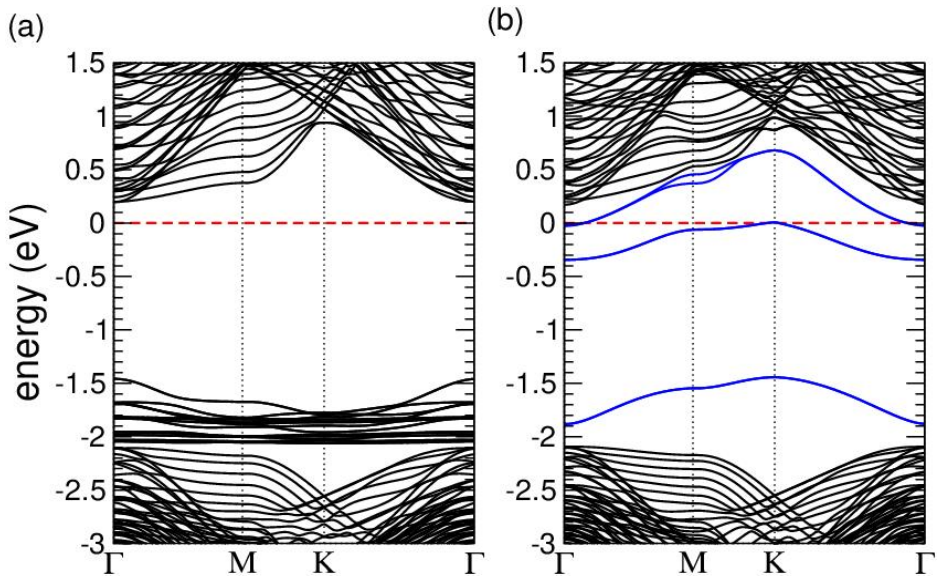

Figure 6: Band structure plots of the (111) ETO/STO interface; (a) and (b) represent spin-majority and spin-minority channels. Red dashed line is the Fermi energy (taken as zero energy). In blue are the bands which host the 2DEG. This is entirely included in the spin-minority channel, i.e. the gas is fully polarized and half-metallic; since the Eu 4*f* magnetic moments are upward oriented, the material is FiM overall.

CONCLUSIONS

We performed GGA+U calculations to analyze the (111) termination of two materials, i.e. the prototypical oxide STO, and the ETO/LAO interface, which is, at our knowledge, the only heterostructure where clear signature of magnetically ordered 2DEG was observed. The high polarity of the (111) termination causes a conceptual inconsistency between experiments and ab-initio supercell calculations: the former typically consider a few layers of the polar material grown on-top of an electrostatically neutralized substrate; the latter, when carried out for stoichiometric multilayers, imply spurious built-in electric fields and the coupling of different terminations. Here we circumvent these hurdles using smart atomic structures capable to mimic electrostatically neutralized, doped terminations. This allows us to reproduce the key experimental conditions, i.e. absence of macroscopic field inside the substrate and surface effects related to a single, specific termination. Our calculations show that the high polarity condition is very effective in generating a strong, intrinsic tendency to carrier confinement at the surface for both *p*-type and *n*-type terminations: both hole and electron gases are confined in a few layers nearby the surface. The holes are accommodated by a broad admixture of fully

spin-polarized Eu 4*f* and O 2*p* states, while the electrons reside in Ti 3*d* orbitals, antiferromagnetically coupled to the spin-majority Eu 4*f* magnetic moments. These results leave us to envision a robustly spin-polarized, mobile hole and electron gases. Spin-polarization arises from strong confinement, which induces large exchange splitting in the bands hosting the gas. Since exchange splitting are far larger than the bandwidth, both *p*-type and *n*-type terminations are fully spin-polarized and half-metallic. For what concerns long-range magnetic order, we do not report the evaluation of exchange interactions (which by far exceeds the limit of our computational capability). Nevertheless, all the experimental evidence available for *n*-doped ETO[53-58] and ETO-based (001), (110), and (111) heterostructures[12-21] concordantly envisages FM order, thus furnishing substantial ground to our theoretical description. Alas, we should point out that the presence of defects, not included in our simulations, may severely disrupt this scenario: recent works reporting the direct observation of hole gas in oxide heterostructures[10,11] furnish clear evidence that ionic point defects, especially oxygen vacancies in proximity of the hole confinement region, are dramatically effective in erasing the hole gas. Achieving defect control in these materials is clearly the most crucial challenge in the route towards the actual development of an oxide-based spintronics.

Supporting Information

The Supporting Information is available free of charge at…

Results for the Ti-terminated STO (111) surface (Figure S1), results for the TiO-terminated STO (111) surface (Figure S2), layer-by-layer 2DHG charge distribution (Table S1) and 2DEG charge distribution (Table S2)

Acknowledgements

Work supported by projects PRIN 2017 “TOPSPIN”, and project PRIN 2022 “TOTEM”, funded by Italian Ministry of University and Research (MIUR).

REFERENCES

1) Ohtomo, A.; Hwang, H. Y. A High-Mobility Electron Gas at the LaAlO3/SrTiO3 Heterointerface. *Nature* **2004**, *427*, 423–426.
2) Nakagawa, N.; Hwang, H. Y.; Muller, D. A. Why Some Interfaces Cannot Be Sharp. *Nat. Mater.* **2006**, *5*, 204–209.
3) Huijben, M.; Rijnders, G.; Blank, D. H. A.; Bals, S.; Aert, S. V.; Verbeeck, J.; Tendeloo, G. V.; Brinkman, A.; Hilgenkamp, H. Electronically Coupled Complementary Interfaces between Perovskite Band Insulators. *Nat. Mater.* **2006**, *5*, 556–560.
4) Reyren, N.; Thiel, S.; Caviglia, A. D.; Kourkoutis, L. F.; Hammerl, G.; Richter, C.; Schneider, C. W.; Kopp, T.; Rüetschi, A.-S.; Jaccard, D.; Gabay, M.; Muller, D. A.; Triscone, J.-M.; Mannhart, J. Superconducting Interfaces Between Insulating Oxides. *Science* **2007**, *317*, 1196–1199.
5) Ueno, K.; Nakamura, S.; Shimotani, H.; Ohtomo, A.; Kimura, N.; Nojima, T.; Aoki, H.; Iwasa, Y.; Kawasaki, M. Electric-Field-Induced Superconductivity in an Insulator. *Nat. Mater.* **2008**, *7*, 855–858.
6) Brinkman, A.; Huijben, M.; van Zalk, M.; Huijben, J.; Zeitler, U.; Maan, J. C.; van der Wiel, W. G.; Rijnders, G.; Blank, D. H. A.; Hilgenkamp, H. Magnetic Effects at the Interface between Non-Magnetic Oxides. *Nat. Mater.* **2007**, *6*, 493–496.
7) Caviglia, A. D.; Gabay, M.; Gariglio, S.; Reyren, N.; Cancellieri, C.; Triscone, J.-M. Tunable Rashba Spin-Orbit Interaction at Oxide Interfaces. *Phys. Rev. Lett.* **2010**, *104*, 126803.
8) Pentcheva, R.; Huijben, M.; Otte, K.; Pickett, W. E.; Kleibeuker, J. E.; Huijben, J.; Boschker, H.; Kockmann, D.; Siemons, W.; Koster, G.; Zandvliet, H. J. W.; Rijnders, G.; Blank, D. H. A.; Hilgenkamp, H.; Brinkman, A. Parallel Electron-Hole Bilayer Conductivity from Electronic Interface Reconstruction. *Phys. Rev. Lett*. **2010**, *104*, 166804.
9) Huijben, M.; Kockmann, D.; Huijben, J.; Kleibeuker, J. E.; van Houselt, A.; Koster, G.; Blank, D. H. A.; Hilgenkamp, H.; Rijnders, G.; Brinkman, A.; Zandvliet, H. J. W. Local probing of coupled interfaces between two-dimensional electron and hole gases in oxide heterostructures by variable-temperature scanning tunneling spectroscopy. *Phy. Rev. B* **2012**, *86*, 035140.
10) Lee, H.; Campbell, N.; Lee, J.; Asel, T. J.; Paudel, T. R.; Zhou, H.; Lee, J. W.; Noesges, B.; Seo, J.; Park, B.; Brillson, L. J.; Oh, S. H.; Tsymbal, E. Y.; Rzchowski, M. S.; Eom, C. B. Direct Observation of a Two-Dimensional Hole Gas at Oxide Interfaces. *Nat. Mater.* **2018**, *17*, 231–236.
11) Anh, L. D.; Kaneta, S.; Tokunaga, M.; Seki, M.; Tabata, H.; Tanaka, M.; Ohya, S. High-Mobility 2D Hole Gas at a $SrTiO_3$ Interface. *Adv. Mater.* **2020**, *32*, 1906003.
12) De Luca, G. M.; Di Capua, R.; Di Gennaro, E.; Miletto Granozio, F.; Stornaiuolo, D.; Salluzzo, M. Transport properties of a quasi-two-dimensional electron system formed in $LaAlO_3/EuTiO_3/SrTiO_3$ heterostructures, *Phys. Rev. B* **2014**, *89*, 224413.
13) Stornaiuolo, D.; Cantoni, C.; De Luca, G. M.; Di Capua, R.; Di Gennaro, E.; Ghiringhelli, G.; Jouault, B.; Marrè, D.; Massarotti, D.; Miletto Granozio, F.; Pallecchi, I.; Piamonteze, C.; Rusponi, S.; Tafuri, F.; Salluzzo, M. Tunable spin polarization and superconductivity in engineered oxide interfaces, *Nature Mater*. **2016**, *15*, 278-284.
14) Stornaiuolo, D.; Jouault, B.; Di Gennaro, E.; Sambri, A.; D'Antuono, M.; Massarotti, D.; Miletto Granozio, F.; Di Capua, R.; De Luca, G. M.; Pepe, G. P.; Tafuri, F.; Salluzzo, M. Interplay between spin-orbit coupling and ferromagnetism in magnetotransport properties of a spin-polarized oxide two-dimensional electron

system, *Phys. Rev. B* **2018**, 98, 075409.
15) Di Capua, R.; Verma, M.; Radovic, M.; Strocov, V. M.; Piamonteze, C.; Guedes, E. B.; Plumb, N. C.; Chen, Y.; D'Antuono, M.; De Luca, G. M.; Di Gennaro, E.; Stornaiuolo, D.; Preziosi, D.; Jouault, B.; Miletto Granozio, F.; Sambri, A.; Pentcheva, R.; Ghiringhelli, G.; Salluzzo, M. Orbital selective switching of ferromagnetism in an oxide quasi two-dimensional electron gas, *npj Quantum Materials*, **2022**, *7*, 41.
16) Wadhwa, P.; Bosin, A.; Filippetti, A. Ultra-Thin Magnetic Film with Giant Phonon-Drag for Heat to Spin Current Conversion. *Mater. Horiz.* **2023**, *10*, 3559.
17) Di Capua, R.; Verma, M.; Radović, M.; Plumb, N. C.; Dil, J. H.; Ristić, Z.; Guedes, E. B.; De Luca, G. M.; Preziosi, D.; Wang, Z.; Weber, A. P.; Pentcheva, R.; Salluzzo, M. Two-Dimensional Electron Gas at the (001) Surface of Ferromagnetic $EuTiO_3$. *Phys. Rev. Res.* **2021**, *3*, L042038.
18) Wang, Z.-C.; Zhang, Y.; Li, Z.-N.; Li, S.-S.; Ying, J.-S.; Yan, W.; Chen, L.; Zhang, S.-J.; Luo, F.-S.; Zhao, W.; Ye, M.; Zheng, R.-K. High-mobility spin-polarized two-dimensional electron gas at the interface of EuTiO3/SrTiO3 heterostructures. J. *Phys.: Condens. Matter* **2024**, *36*, 015001
19) Wang, Z.-C.; Li, Z.-N.; Ye, M.; Zhao, W.; Zheng, R.-K. High-mobility spin-polarized quasi-two-dimensional electron gas and large low-field magnetoresistance at the interface of $EuTiO_3/SrTiO_3$ (110) heterostructures. *APL Mater*. **2024**, *12*, 031107.
20) De Luca, G. M.; Di Capua, R.; Di Gennaro, E.; Sambri, A.; Miletto Granozio, F.; Ghiringhelli, G.; Betto, D.; Piamonteze, C.; Brookes, N. B.; Salluzzo, M. Symmetry breaking at the (111) interfaces of $SrTiO_3$ hosting a two-dimensional electron system. *Phys. Rev. B* **2018**, *98*, 115143.
21) Chen, Y.; D'Antuono, M.; Brookes, N. B.; De Luca, G. M.; Di Capua, R.; Di Gennaro, E.; Ghiringhelli, G.; Piamonteze, C.; Preziosi, D.; Jouault, B.; Cabero, M.; González-Calbet, J. M.; León, C.; Santamaria, J.; Sambri, A.; Stornaiuolo, D.; Salluzzo, M. Ferromagnetic Quasi-Two-Dimensional Electron Gas with Trigonal Crystal Field Splitting. *ACS Appl. Electron. Mater*. **2022**, *4*, 3226−3231
22) Meevasana, W.; King, P. D. C.; He, R. H.; Mo, S.-K.; Hashimoto, M.; Tamai, A.; Songsiriritthigul, P.; Baumberger, F.; Shen, Z.-X. Creation and Control of a Two-Dimensional Electron Liquid at the Bare $SrTiO_3$ Surface. *Nat. Mater.* **2011**, *10*, 114–118.
23) Santander-Syro, A. F.; Copie, O.; Kondo, T.; Fortuna, F.; Pailhès, S.; Weht, R.; Qiu, X. G.; Bertran, F.; Nicolaou, A.; Taleb-Ibrahimi, A.; Le Fèvre, P.; Herranz, G.; Bibes, M.; Reyren, N.; Apertet, Y.; Lecoeur, P.; Barthélémy, A.; Rozenberg, M. J. Two-Dimensional Electron Gas with Universal Subbands at the Surface of $SrTiO_3$. *Nature* **2011**, *469*, 189–193.
24) Wang, Z.; Zhong, Z.; Hao, X.; Gerhold, S.; Stöger, B.; Schmid, M.; Sánchez-Barriga, J.; Varykhalov, A.; Franchini, C.; Held, K.; Diebold, U. Anisotropic Two-Dimensional Electron Gas at $SrTiO_3$ (110). *Proc. Natl. Acad. Sci.* **2014**, *111*, 3933–3937.
25) Delugas, P.; Fiorentini, V.; Mattoni, A.; Filippetti, A. Intrinsic origin of two-dimensional electron gas at the (001) surface of $SrTiO_3$. *Phys. Rev. B* **2015**, *91*, 115315.
26) Russell, B. C.; Castell, M. R. $(\sqrt{13}\times\sqrt{13})R13.9°$ and $(\sqrt{7}\times\sqrt{7})R19.1°$ reconstructions of the polar $SrTiO_3$ (111) surface. *Phys. Rev. B* **2007**, *75*, 155433.
27) Chiaramonti, A. N.; Lanier, C. H.; Marks, L. D.; Stair, P. C. Time, temperature, and oxygen partial pressure-dependent surface reconstructions on $SrTiO_3$ (111): A systematic study of oxygen-rich conditions. *Surface Science* **2008**, *602*, 3018–3025
28) Feng, J.; Zhu, X.; Guo, J. Reconstructions on $SrTiO_3$ (111) surface tuned by Ti/Sr deposition. *Surface Science* **2013**, *614*, 38–45.
29) Tanaka, H.; Kawai, T. Surface Structure of Reduced $SrTiO_3$ (111) Observed by Scanning Tunneling Microscopy. *Surf. Sci.* **1996**, *365*, 437–442.

30) Biswas, A.; Rossen, P. B.; Yang, C.-H.; Siemons, W.; Jung, M.-H.; Yang, I. K.; Ramesh, R.; Jeong, Y. H. Universal Ti-Rich Termination of Atomically Flat $SrTiO_3$ (001), (110), and (111) Surfaces. *Appl. Phys. Lett.* **2011**, *98*, 051904.
31) Saghayezhian, M.; Chen, L.; Wang, G.; Guo, H.; Plummer, E. W.; Zhang, J. Polar compensation at the surface of $SrTiO_3$ (111). *Phys. Rev. B* **2016**, *93*, 125408.
32) Torrelles, X.; Cantele, G.; De Luca, G. M.; Di Capua, R.; Drnec, J.; Felici, R.; Ninno, D.; Herranz, G.; Salluzzo, M. Electronic and Structural Reconstructions of the Polar (111) $SrTiO_3$ Surface. *Phys. Rev. B* **2019**, *99*, 205421.
33) Rödel, T. C.; Bareille, C.; Fortuna, F.; Baumier, C.; Bertran, F.; Le Fèvre, P.; Gabay, M.; Hijano Cubelos, O.; Rozenberg, M. J.; Maroutian, T.; Lecoeur, P.; Santander-Syro, A. F. Orientational Tuning of the Fermi Sea of Confined Electrons at the $SrTiO_3$ (110) and (111) Surfaces. *Phys. Rev. Appl*. **2014**, *1*, 051002.
34) McKeown Walker, S.; de la Torre, A.; Bruno, F. Y.; Tamai, A.; Kim, T. K.; Hoesch, M.; Shi, M.; Bahramy, M. S.; King, D. C.; Baumberger, F. Control of a Two-Dimensional Electron Gas on $SrTiO_3$ (111) by Atomic Oxygen. *Phys. Rev. Lett*. **2014**, *113*, 177601.
35) He, P.; McKeown Walker, S.; Zhang, S.-L.; Bruno, F. Y.; Bahramy, M. S.; Lee, J. M.; Ramaswamy, R.; Cai, K.; Heinonen, O.; Vignale, G.; Baumberger, F.; Yang, H. Observation of Out-of-Plane Spin Texture in a $SrTiO_3$ (111) Two-Dimensional Electron Gas. *Phys. Rev. Lett*. **2018**, *120*, 266802.
36) Miao, L.; Du, R.; Yin, Y.; Li, Q. Anisotropic magneto-transport properties of electron gases at SrTiO3 (111) and (110) surfaces. *Appl. Phys. Lett*. **2016**, *109*, 261604.
37) Herranz, G.; Sanchez, F.; Dix, N.; Scigaj, M.; Fontcuberta, J. High mobility conduction at (110) and (111) $LaAlO_3/SrTiO_3$ interfaces. *Sci. Rep*. **2012**, *2*, 758.
38) Rout, P. K.; Agireen, I.; Maniv, E.; Goldstein, M.; Dagan, Y. Six-fold crystalline anisotropic magnetoresistance in the (111) $LaAlO_3/SrTiO_3$ oxide interface. *Phys. Rev. B* **2017**, *95*, 241107(R).
39) Davis, S.; Huang, Z.; Han, K.; Ariando, A.; Venkatesan, T.; Chandrasekhar, V. Anisotropic superconductivity and frozen electronic states at the (111) $LaAlO_3/SrTiO_3$ interface. *Phys. Rev. B* **2018**, *98*, 024504.
40) Khanna, U.; Rout, P. K.; Mograbi, M.; Tuvia, G.; Leermakers, I.; Zeitler, U.; Dagan, Y.; Goldstein, M. Symmetry and Correlation Effects on Band Structure Explain the Anomalous Transport Properties of (111) $LaAlO_3/SrTiO_3$. *Phys. Rev. Lett*. **2019**, *123*, 036805.
41) Monteiro, A. M. R. V. L.; Vivek, M.; Groenendijk, D. J.; Bruneel, P.; Leermakers, I.; Zeitler, U.; Gabay, M.; Caviglia, A. D. Band inversion driven by electronic correlations at the (111) $LaAlO_3/SrTiO_3$ interface. *Phys. Rev. B* **2019**, *99*, 201102(R).
42) Lesne, E.; Sağlam, Y. G.; Battilomo, R.; Mercaldo, M. T.; van Thiel, T. C.; Filippozzi, U.; Noce, C.; Cuoco, M.; Steele, G. A.; Ortix, C.; Caviglia, A. D. Designing spin and orbital sources of Berry curvature at oxide interfaces. *Nat. Mater*. **2023**, *22*, 576–582.
43) Anderson, T. J.; Zhou, H.; Xie, L.; Podkaminer, J. P.; Patzner, J. J.; Ryu, S.; Pan, X. Q.; Eom, C. B. Interfacial B-site atomic configuration in polar (111) and non-polar (001) $SrIrO_3/SrTiO_3$ heterostructures. *APL Mater*. **2017**, *5*, 096110.
44) Marks, L. D.; Chiaramonti, A. N.; Tran, F.; Blaha, P. The small unit cell reconstructions of $SrTiO_3$ (111). *Surface Science* **2009**, *603*, 2179–2187.
45) Pojani, A.; Finocchi, F.; Noguera, C. Polarity on the $SrTiO_3$ (111) and (110) surfaces. *Surf. Sci*. **1999**, *442*, 179–198.
46) Sivadas, N.; Dixit, H.; Cooper, V. R.; Xiao, D. Thickness-Dependent Carrier Density at the Surface of $SrTiO_3$ (111) Slabs. *Phys. Rev. B* **2014**, *89*, 075303.
47) Yin, Y.; Wang, J.; Zhu, H.; Lv, K.; Wu, X. S. Structural Distortion and Charge Redistribution in $SrTiO_3$ (111) Polar Surfaces. *Vacuum* **2015**, *120*, 83–88.

48) Herranz, G.; Sanchez, F.; Dix, N.; Scigaj, M.; Fontcuberta, J. High mobility conduction at (110) and (111) $LaAlO_3/SrTiO_3$ interfaces. *Sci. Rep*. **2012**, *2*, 758.
49) Doennig, D.; Pickett, W. E.; Pentcheva, R. Massive Symmetry Breaking in $LaAlO_3/SrTiO_3$ (111) QuantumWells: A Three-Orbital Strongly Correlated Generalization of Graphene. *Phys. Rev. Lett*. **2013**, *111*, 126804.
50) Trama, M.; Cataudella, V.; Perroni, C. A.; Romeo, F.; Citro, R. Effect of Confinement and Coulomb Interactions on the Electronic Structure of the (111) $LaAlO_3/SrTiO_3$ Interface. *Nanomaterials* **2023**, *13*, 819.
51) Rüegg, A.; Fiete, G. A. Topological Insulators from Complex Orbital Order in Transition-Metal Oxides Heterostructures. *Phys. Rev. B* **2011**, *84*, 201103.
52) Okamoto, S. Doped Mott Insulators in (111) Bilayers of Perovskite Transition-Metal Oxides with a Strong Spin-Orbit Coupling. *Phys. Rev. Lett.* **2013**, *110*, 066403.
53) Katsufuji, T.; Tokura, Y. Transport and Magnetic Properties of a Ferromagnetic Metal: $Eu_{1-x}R_xTiO_3$. *Phys. Rev. B* **1999**, *60*, 15021–15023.
54) Li, L.; Zhou, H.; Yan, J.; Mandrus, D.; Keppens, V. Research Update: Magnetic Phase Diagram of $EuTi_{1-x}B_xO_3$ (B = Zr, Nb). *APL Mater.* **2014**, *2*, 110701.
55) Li, L.; Morris, J. R.; Koehler, M. R.; Dun, Z.; Zhou, H.; Yan, J.; Mandrus, D.; Keppens, V. Structural and Magnetic Phase Transitions in $EuTi_{1-x}Nb_xO_3$. *Phys. Rev. B* **2015**, *92*, 024109.
56) Yamamoto, T.; Yoshii, R.; Bouilly, G.; Kobayashi, Y.; Fujita, K.; Kususe, Y.; Matsushita, Y.; Tanaka, K.; Kageyama, H. An Antiferro-to-Ferromagnetic Transition in $EuTiO_{3-x}H_x$ Induced by Hydride Substitution. *Inorg. Chem.* **2015**, *54*, 1501–1507.
57) Ahadi, K.; Gui, Z.; Porter, Z.; Lynn, J. W.; Xu, Z.; Wilson, S. D.; Janotti, A.; Stemmer, S. Carrier Density Control of Magnetism and Berry Phases in Doped $EuTiO_3$. *APL Mater.* **2018**, *6*, 056105.
58) Takahashi, K. S.; Ishizuka, H.; Murata, T.; Wang, Q. Y.; Tokura, Y.; Nagaosa, N.; Kawasaki, M. Anomalous Hall Effect Derived from Multiple Weyl Nodes in High-Mobility $EuTiO_3$ Films. *Sci. Adv.* **2018**, *4*, eaar7880.
59) Gui, Z.; Janotti, A. Carrier-Density-Induced Ferromagnetism in $EuTiO_3$ Bulk and Heterostructures. *Phys. Rev. Lett.* **2019**, *123*, 127201.
60) Wadhwa, P.; Bosin, A.; Filippetti, A. Giant Spin-Dependent Seebeck Effect from Fully Spin-Polarized Carriers in n-doped $EuTiO_3$: A Prototype Material for Spin-Caloritronic Applications. *J. Mater. Chem. A* **2023**, *11*, 6842–6853.
61) Kresse, G.; Furthmüller, J. Efficient Iterative Schemes for *Ab Initio* Total-Energy Calculations Using a Plane-Wave Basis Set. *Phys. Rev. B* **1996**, *54*, 11169–11186.
62) Kresse, G.; Joubert, D. From Ultrasoft Pseudopotentials to the Projector Augmented-Wave Method. *Phys. Rev. B* **1999**, *59*, 1758–1775.
63) Perdew, J. P.; Burke, K.; Ernzerhof, M. Generalized Gradient Approximation Made Simple. *Phys. Rev. Lett.* **1996**, *77*, 3865–3868.
64) Anisimov, V. I.; Zaanen, J.; Andersen, O. K. Band Theory and Mott Insulators: Hubbard *U* Instead of Stoner *I*. *Phys. Rev. B* **1991**, *44*, 943–954.
65) Gazquez, J.; Stengel, M.; Mishra, R.; Scigaj, M.; Varela, M.; Roldan, M. A.; Fontcuberta, J.; Sánchez, F.; Herranz, G. Competition between Polar and Nonpolar Lattice Distortions in Oxide Quantum Wells: New Critical Thickness at Polar Interfaces. Phys. Rev. Lett. **2017**, *119*, 106102.
66) Bussmann-Holder, A.; Köhler, J. Revisiting the fascinating properties of $EuTiO_3$ and ist mixed crystals with $SrTiO_3$: Possible candidates for novel functionalities. *J. Phys. Chem. Solids* **2015**, *84*, 2–12.
67) Stengel, M. First-Principles Modeling of Electrostatically Doped Perovskite Systems. *Phys. Rev. Lett*. **2011**, *106*, 136803.

68) Loos, J.: Novak, P. Double exchange and superexchange in a ferrimagnetic half-metal. *Phys. Rev. B* **2002**, *66*, 132403.

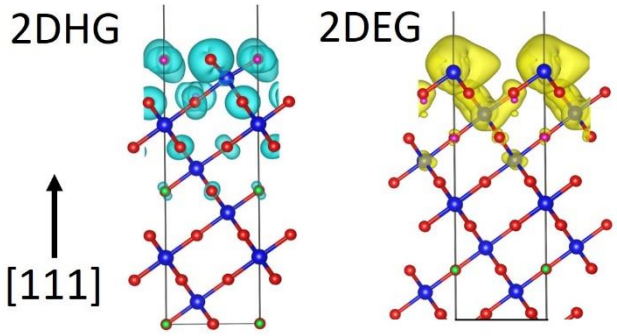

For Table of Contents Use Only